







RESEARCH ARTICLE | AUGUST 02 2024

Hybrid use of a robotic welding system in remote laser separation of thin-sheet Al casings for the recycling of battery packs

Special Collection: [Laser Manufacturing for Future Mobility](#)

Simone D'Arcangelo  ; Matteo Busatto  ; Leonardo Caprio   ; Barbara Previtali  ; Ali Gökhan Demir 



J. Laser Appl. 36, 032023 (2024)






<https://doi.org/10.2351/7.0001359>



ALIA
THE LASER INSTITUTE

**Journal of
Laser Applications**

[Learn More](#)

-  **RAPID TIME TO ACCEPTANCE**
-  **COMMUNITY DRIVEN**
-  **EXPANSIVE COVERAGE**
-  **PRESTIGIOUS EDITORIAL BOARD**
-  **EXTENSIVE MARKETING**

Hybrid use of a robotic welding system in remote laser separation of thin-sheet Al casings for the recycling of battery packs

Cite as: J. Laser Appl. 36, 032023 (2024); doi: 10.2351/7.0001359

Submitted: 28 February 2024 · Accepted: 15 July 2024 ·

Published Online: 2 August 2024



Simone D'Arcangelo,  Matteo Busatto,  Leonardo Caprio, ^{a)}  Barbara Previtali,  and Ali Gökhan Demir 

AFFILIATIONS

Department of Mechanical Engineering, Politecnico di Milano, Via La Masa 1, 20156 Milan, Italy

Note: Paper published as part of the special topic on Laser Manufacturing for Future Mobility

^{a)} Author to whom correspondence should be addressed; electronic mail: leonardo.caprio@polimi.it

ABSTRACT

Robotic systems equipped with high-power laser sources are often employed for the production of battery packs for the electric mobility sector. Considering the strive toward a circular manufacturing economy, there is great interest in the possibility of reconfiguring such equipment for dismantling operations. The present study explores the hybrid use of a robotized fiber laser welding system, adapting its scope from joining of battery casings toward the separation of the same thin Al sheets, enabling the recycling of the internal cells of the battery pack. Process feasibility is assessed by tailoring the beam size as well as exploiting dynamic beam oscillation to perform the separation process. Dynamic beam oscillation allows us to obtain a smaller kerf width and greater process stability with respect to linear trajectories with larger beam sizes. The damage to underlying cells of the separation region was also assessed on different materials (Al, Ni-plated steel, and Cu). Greater surface modifications and higher peak temperatures (in excess of 800 °C) were recorded when employing dynamic beam oscillation with respect to linear trajectories. This research demonstrates a pathway for reutilization of the existing technological systems for a circular and sustainable production chain in the e-mobility sector.

Key words: laser cutting, demanufacturing, recycling, electric mobility

© 2024 Author(s). All article content, except where otherwise noted, is licensed under a Creative Commons Attribution (CC BY) license (<https://creativecommons.org/licenses/by/4.0/>). <https://doi.org/10.2351/7.0001359>

I. INTRODUCTION

As the electrification of vehicles continues, the use of battery packs for traction system applications increases. These consist of several Li-ion cells connected via busbars, encased and sealed in the containing pack. Laser-based manufacturing processes are industrially used to produce the components of the battery pack.¹ Laser cutting is used for slitting and forming Li-ion electrodes. Laser welding is used to assemble the electrodes, seal the cell cans, provide electrical connections with busbars, and seal the battery pack. As the number of electric vehicles in use increases and the existing vehicles in circulation age, the necessity to recycle and reuse the battery cells inside them becomes more evident. Laser systems used for producing the battery pack can also be potentially used in the recycling stage for reopening them as indicated by

Rettenmeier *et al.*² The laser systems employed in welding processes usually operate with beam sizes in the range of 100–300 μm, often manipulated by scanning optics for beam oscillation and steering. The same optical chain could be potentially used for remote material separation. Figure 1(a) shows the remote laser separation process for the opening of battery packs. These are commonly produced using lightweight metals such as Al alloys with a 1–2 mm thickness.

Remote ablation cutting can be employed for the processing of thin metallic sheets such as battery foil electrodes, a rising topic within the current transition to electric mobility.³ Various solutions have been explored in literature employing both ns-pulsed and ultrafast laser sources as in the research works by Lutey *et al.* and by Zhang *et al.*^{4–6} Different emission wavelengths may be exploited to improve the quality finish as shown by Demir and Previtali.⁷

26 August 2024 08:11:47

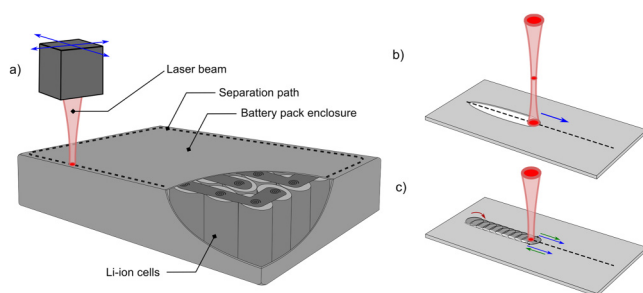


FIG. 1. (a) Schematic description of remote laser separation used on battery packs. (b) The use of a defocused beam on a linear trajectory. (c) The use of a focused beam oscillating with a circular pattern.

This process may also be conducted with high-brilliance CW laser systems that are competitive in terms of productivity as shown by Kriegler *et al.* and Patwa *et al.*^{8,9} Lee *et al.* also contributed significantly in studying the slitting of thin sheets with CW fiber laser sources.^{10–12} Burst mode emission of the ps-pulsed laser source is another promising solution to improve cut quality and productivity as indicated by Huang *et al.*¹³ However, when employing pulsed laser sources, the process efficiency significantly reduces with an increase in the material thickness, especially when considering typical values of battery casings in the millimeter range.¹⁴

Laser cutting with a process gas conventionally operates with a melt and blow mechanism.¹⁵ The laser beam generates the melting of the material, which is pushed down from the opened kerf. In the absence of a process gas to achieve the blowing action, the process moves to a remote cutting configuration. Research has concentrated on improving the cut quality with limited thickness (<1 mm) using high-quality beam sources such as single-mode fiber lasers.^{16–19} Elevated cut speeds have been enabled by the introduction of high-brightness fiber laser sources.²⁰ In the case of a laser beam typically used for welding operations, material separation may move away from high-quality cutting via vapor-dominant material expulsion. On the other hand, such beams can be potentially used for material removal by melt expulsion, providing a separation without the need for high-quality kerfs. In this processing regime, the laser beam is expected to penetrate through the entire thickness of the battery pack layer and the excess beam to reach the underlying connection busbars as well as the battery cells themselves. The damage provided by the excess beam on the underlying materials has to be evaluated for safety as well as material recoverability.

In literature, there is evidence regarding the use of high-power laser sources for dismantling or cutting operations. The first studies on the topic were reported by the research group of Gladush and co-workers, which exploited a high-power CO₂ laser source for remote cutting operations.²¹ The technique under study was implemented for the dismantling of high-thickness steel structures²² including modeling of the melting mechanism.²³ Brodesser *et al.* showed the development of a mobile fiber laser cutting system.²⁴ Choubey *et al.* studied the use of a pulsed Nd:YAG laser for dismantling operations using a proximity cutting head in both dry air

and underwater environments.²⁵ Villumsen *et al.* extensively investigate robotized remote cutting operations, exploiting a fiber laser and diffractive optical elements to shape the beam to enhance the process functionality.^{26–29} Researchers from IWS Dresden also explored the use of remote fusion cutting for the processing of steel sheets in the millimeter range^{30,31} as well as the IWB group at the Technical University of Munich.³² Specific attention was devoted to characterizing the cut kerf geometry as well as the trajectory planning of robotized systems for remote fusion cutting.^{33,34}

Although high-power solid-state laser sources emitting with continuous wave emission have been studied extensively for remote separation processes, the use of beam shaping techniques has been analyzed limitedly. Villumsen and co-workers explored the possibility of employing a diffractive optical element to modify the power emission profile.^{26,27} Dynamic beam shaping approaches to tailor the distribution of the laser emission power are among the promising solutions to enhance process productivity and quality during laser cutting. Researchers from KU Leuven have explored the possibility of oscillating the beam during the processing of high-thickness materials.^{35–38} Research activities on these techniques are also explored at IWS Dresden.^{39,40} Although material thicknesses are uncommon for the current battery pack casings, the possibility of employing dynamic beam oscillation to improve the dismantling process with remote processing operations remains a scientifically relevant question.

The possibility of employing fiber laser cutting systems for the dismantling of battery packs has been hypothesized by Kampker *et al.*, given their intrinsic flexibility and reconfigurability.⁴¹ Still, this approach has not been analyzed within the scientific literature. Among the open challenges in the remanufacturing processes reside the risks associated to the damaging of the cells within the internal structure of the battery pack. Ad-hoc design of the battery packs could enable easier demanufacturing; yet, given the wide variety of battery systems in terms of shape and geometry, it is of interest to explore the effect that laser-based material separation strategies could have on their internal contents. Accordingly, this work studies the remote laser separation process for recycling battery packs by exploiting a reconfigurable robotized system, which enables flexible planning and design of operations and processing conditions. A fiber laser source used for laser welding operations was adapted to this process. Al-alloy thin sheets were processed using a defocused beam and linear trajectory [Fig. 1(b)] as well as a focused and oscillating beam [Fig. 1(c)]. Within the identified operating windows, experiments were conducted to assess damage to the underlying materials. Temperature rise on the busbar materials was also measured. Conventionally used materials such as Ni-coated steel, Al, and Cu were employed. The results are interpreted for a better understanding of the separation process and correct usage in the battery pack dismantling procedures.

II. MATERIALS AND METHODS

A. Laser system

The remote separation process was carried out using a robotic laser system mainly employed for laser welding with beam oscillation (BLM Group, Italy). The experimental system was

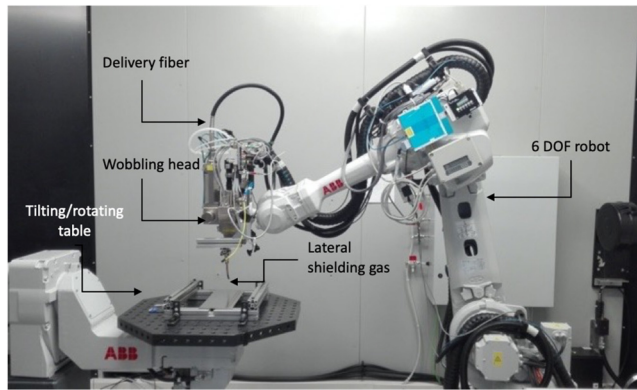


FIG. 2. Robotic laser welding system used in the experimental study.

representative of a laser welding system that may be adapted to battery pack recycling operations. It consisted of a six-degree-of-freedom robotic arm and a two-degree-of-freedom rotary/tilting table as shown in Fig. 2. The robotized configuration of the welding system is a fundamental to enable the reconfigurability of the production system from a manufacturing to a dismantling system. This setup allows us to digitally replan the processing trajectories, guarantees full accessibility to different geometries and positions, and modifies the processing conditions by regulating the working distance between the welding head and the process parameters related to the laser beam.

A 6-kW multimode active fiber laser with 100 μm delivery fiber was employed (IPG YLP 6000, Oxford, MA). The laser source was coupled to a wobble head capable of oscillating the beam in various trajectories with up to 500 Hz frequency and 3 mm amplitude (IPG D50, Oxford, MA). The optical path consisted of a 200 mm collimating and a 300 mm focusing lens producing a 150 μm beam waist diameter. Table I summarizes the main characteristics of the laser system.

B. Materials

Aluminum alloy grade EN AW 6061 with 1 mm thickness was used as the material to be separated representing the casing material of a battery pack. It was used in cold-rolled conditions. As

TABLE I. Main specifications of the laser system.

Parameter	Value
Wavelength, λ (nm)	1070
Beam quality factor, M^2	11.2
Available laser power, P (W)	6000
Feeding fiber core diameter, d_f (μm)	100
Focal length, f_f (mm)	300
Collimation length, f_c (mm)	200
Beam waist diameter, d_0 (μm)	150

busbar materials, high purity Al with 0.8 mm thickness, Ni-coated steel (Hilumin) with 0.3 mm thickness, and pure Cu with 0.2 mm thickness were tested.

C. Measurement equipment

Optical microscopy images of the separation tracks and the damage traces on the busbars were acquired (UM 300 I BD, EchoLAB, Paderno Dugnano, Italy). The temperature rise on the busbars was measured with K thermocouples. The acquisition frequency for the temperature measurement was set to 10 Hz.

III. STUDY OF LASER SEPARATION

A. Impact of beam size with a linear cutting trajectory

The remote separation process was studied employing a linear trajectory in the initial part. The laser beam size plays a critical role in material separation. A small beam may allow us to increase the laser intensity delivered to the workpiece. However, without the blowing action of a process gas, the molten material may resolidify without a consistent separation track. The use of a wider beam may allow for the widening of the molten area and, hence, provide complete material separation in the absence of a process gas. Accordingly, in this experimental campaign, the effect of the beam size was evaluated along with laser power and processing speed. The power level was varied between 4 and 6 kW using speeds between 40 and 80 mm/s. The focal position was varied between 0 and 10 mm above the workpiece surface. In these combinations, the spot sizes were 150 and 1024 μm , respectively. The beam was defocused to a point above the surface to avoid elevated beam irradiance levels on the underlying battery cells in the final application. The process parameters in the linear cutting trajectory experiments are summarized in Table II.

Figure 3 depicts the results of the linear cutting trajectory experiments, where the effect of the varied process parameters on the separation status could be observed. The experiments produced conditions of no separation, unstable separation, and successful separation. The no separation condition consisted of an evident melting process, which subsequently resolidified, forming an inconsistent remolten seam. Such conditions were verified when the smallest beam size, with the focal point on the surface, was employed ($\Delta z = 0$). By enlarging the beam on the material surface, unstable and separation conditions were achieved. At low-power (4 kW) and high-speed conditions (60–80 mm/s), the tracks were unseparated, following a molten and resolidified morphology similar to those observed with the smallest beam size. With a 5 kW

TABLE II. Fixed and varied parameters for the linear cutting trajectory.

Fixed parameter	Value
Process gas	None
Varied parameters	Value
Power, P (kW)	4, 5, 6,
Speed, v (mm/s)	40, 60, 80
Focal position, Δz (mm)	0, +10

26 August 2024 08:11:47

a) $\Delta z = 0$ mm

P [kW]	v [mm/s]	Macro		5 mm	Separation status
		Top	Root		
4	40				No
	60				No
	80				No
5	40				No
	60				No
	80				No
6	40				No
	60				No
	80				No

b) $\Delta z = +10$ mm

P [kW]	v [mm/s]	Macro		5 mm	Separation status
		Top	Root		
4	40				Unstable
	60				No
	80				No
5	40				Separation
	60				Unstable
	80				Unstable
6	40				Separation
	60				Separation
	80				Separation

FIG. 3. Separation status as a function of power and speed with the spot size (a) on the surface and (b) 10 mm above the surface.

laser power, complete separation was achievable at the lowest speed, while at 6 kW, all conditions produced complete separation. The unstable conditions showed repetitive patterns of the separated material, implying melt pool instability and resolidification behind the separation front. At the lowest energy conditions ($P = 4$ kW, $v = 40$ mm/s), the frequency of this opening and collapsing process is at its highest, with repetitions approximately every 5 mm. Providing more energy ($P = 5$ kW, $v = 60$ and 80 mm/s), the repetition frequency moves to approximately 8 mm.

Figure 4(a) shows the observed qualitative conditions in the parameter's space, while Fig. 4(b) shows the kerf sizes in the stable separation parameter combinations.

It can be seen that the kerf width results are larger than 1 mm for all cases, with values always above the employed beam spot size.

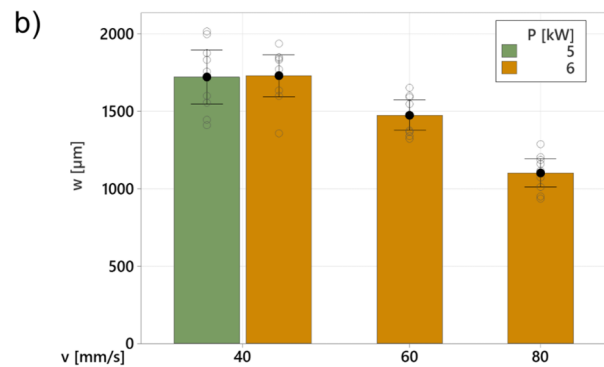
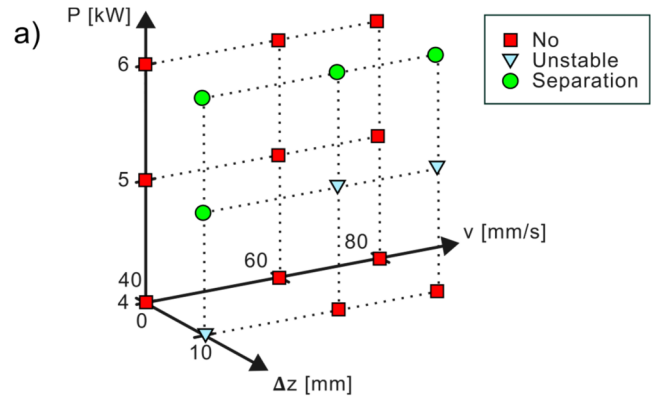


FIG. 4. (a) The resulting feasibility window with a linear trajectory. (b) Kerf width measured in the feasibility window as a function of speed and power at $\Delta z = 10$ mm. Error bars indicate 95% CI.

Metallographic cross sections along the transverse direction of the cuts are shown in Fig. 5. In these conditions, it can be deduced that the separation process is based on material evaporation as well as melt separation due to material surface tension. As a matter of fact, a part of the molten material remains attached to the side of the

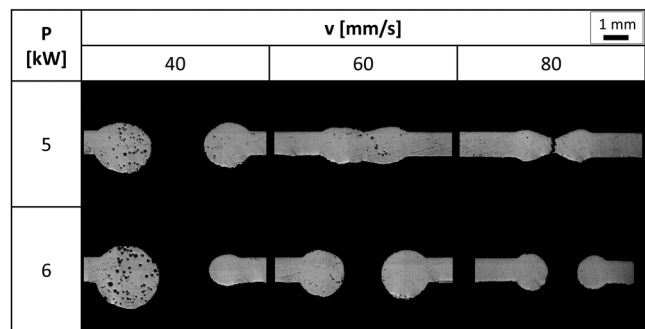


FIG. 5. Metallographic cross sections along the transverse direction of the cuts obtained with a linear cutting trajectory at $\Delta z = +10$ mm. Successful conditions exhibit an open kerf.

26 August 2024 08:11:47

kerf, exhibiting a rounded geometry indicative of the surface tension effects acting on the melt. It is also possible to denote the presence of pores in the resolidified material, typical of gas entrapment that occurs when Al is exposed to the atmosphere at the liquid state at high temperatures. Moreover, heat conduction is expected to play a significant role in enlarging the melt region and facilitating the separation cut, however, at the cost of increasing the heat-affected zone in the vicinity of the kerf.

As a complementary part to the linear trajectory investigation, the remote separation process was also studied with an oscillating laser beam. With a well-focused and oscillating beam, the objective was to facilitate melt expulsion through the wider kerf and the stirring action of the oscillation pattern. In this phase, the power was fixed at 6 kW and the focal position was placed on the material surface, providing the smallest beam size. A circular oscillation pattern with variable amplitude and frequency was superimposed on the linear trajectory. The linear speed was varied between 60 and 100 mm/s. The oscillation amplitude was varied at 0.5 and 1 mm, with frequencies at 150, 300, and 450 Hz. The details of the oscillating beam experiments are summarized in Table III.

Figure 6 shows the separation status as a function of the tested parameters with the oscillating beam. The process feasibility window is shown in Fig. 7(a), while in Fig. 7(b), the kerf width of the successful separation cuts is shown.

The processed tracks exhibit smaller sizes when compared to the linear trajectory conditions, despite the wide oscillation amplitudes. No complete separation was achieved with a 0.5 mm oscillation amplitude, resulting in tracks characterized by intermittent molten and solidified materials, resembling a welding condition. At higher oscillation frequencies of 300 and 450 Hz, along with a 0.5 mm amplitude, the tracks appear unstably separated, suggesting that surface tension and the limited size of the opened kerf do not allow outward material flow. By increasing the oscillation amplitude to 1 mm, complete separation conditions were achieved. At a low frequency of 150 Hz, full separation is observed at the lowest speed, while at higher frequencies, separation was achieved in all tested combinations.

The metallographic cross sections transverse to the cut direction shown in Fig. 8 allow us to observe the kerf geometry. The separated tracks appear to have the solidified material accumulated only on one side. The solidified material is also characterized by the presence of pores, while the other side of the cut does not

TABLE III. Fixed and varied parameters used with the oscillating beam.

Fixed parameters	Value
Power, P (kW)	6
Focal position, Δz (mm)	0
Oscillation pattern	Circular
Process gas	None
Varied parameters	Value
Speed, v (mm/s)	60, 80, 100
Oscillation amplitude, A (mm)	0.5, 1
Oscillation frequency, f (Hz)	150, 300, 450

a) $A = 0.5$ mm

f [Hz]	v [mm/s]	Macro		5 mm	Separation status
		Top	Root		
150	60				No
	80				No
	100				No
300	60				No
	80				Unstable
	100				Unstable
450	60				Unstable
	80				Unstable
	100				Unstable

b) $A = 1$ mm

f [Hz]	v [mm/s]	Macro		5 mm	Separation status
		Top	Root		
150	60				Separation
	80				Unstable
	100				Unstable
300	60				Separation
	80				Separation
	100				Separation
450	60				Separation
	80				Separation
	100				Separation

FIG. 6. Separation status as a function of oscillation frequency and speed with (a) the oscillation amplitude at 0.5 mm and (b) at 1 mm.

exhibit such issues. With the combined feed and oscillation motions, the beam speed increases when the two are aligned in the same direction. Hence, the nonejected material is accumulated on this side. Figure 7(a) collects the different separation statuses observed in the experiments, while Fig. 7(b) shows the kerf width measured in the separation conditions. It can be seen that the kerf is always smaller than the employed oscillation amplitude of 1 mm, confirming once again that the material expulsion is incomplete over the lateral extent of the oscillation. In these conditions, the overall material ejection mechanism is observed to be vaporization and melt expulsion via pressure applied by the keyhole that also enables a smaller heat-affected region similar to the thermal propagation obtained when employing melt and blow-cutting techniques with the aid of the assist gas.

26 August 2024 08:11:47

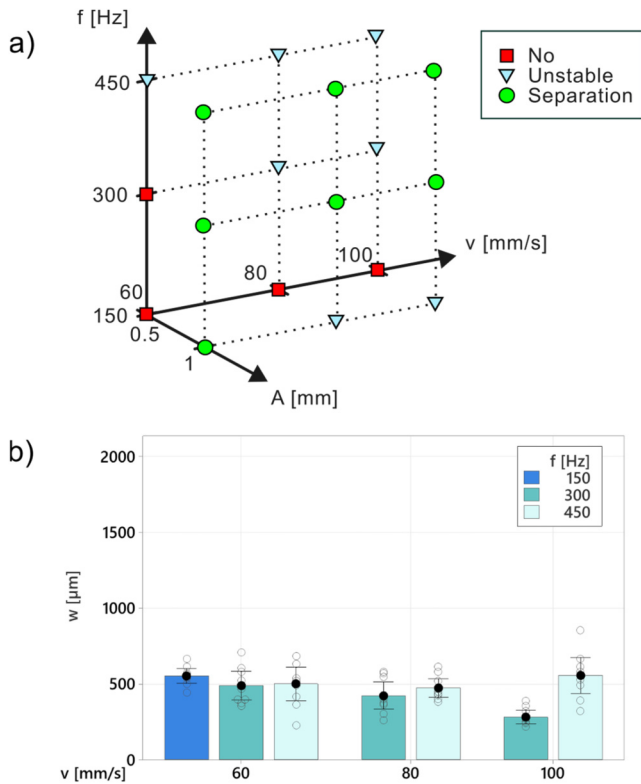


FIG. 7. (a) The resulting feasibility window with circular oscillations superimposed to the linear trajectory. (b) Kerf width measured in the feasibility window as a function of speed and oscillation frequency. Error bars indicate 95% CI.

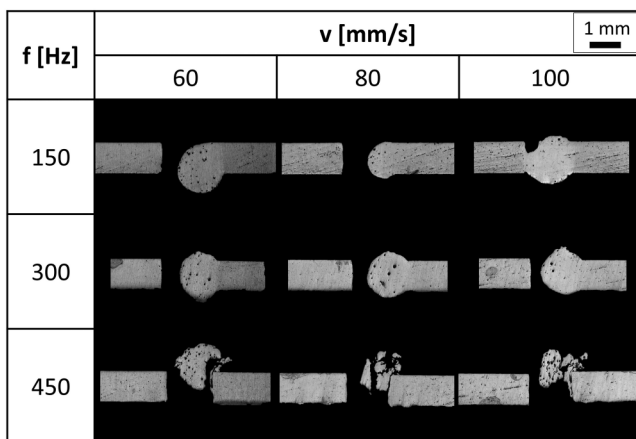


FIG. 8. Metallographic cross sections along the transverse direction of the cuts obtained with a circular trajectory. Successful cut conditions show an open kerf.

IV. EVALUATION OF THE DAMAGE ON THE UNDERLYING BATTERY CELLS

A. Experimental design

The effect of the separation process on the underlying battery cells was evaluated with a dedicated experimental setup simulating the battery pack opening conditions. An empty cylindrical battery cell (46 900 model) was placed under the Al-alloy sheet to be separated with a connector busbar. The distance between the Al-alloy sheet representing the pack and the busbar connector (L) was controlled. Temperatures were acquired on the underlying busbar at 5 mm (channel 1 CH1) and 10 mm (channel 2 CH2) transversally from the center of the linear trajectory of the cut separation path as shown in Fig. 9. The overall experimental arrangement indicating the laser welding system, the foil representative of the battery pack casing, and the underlying cell is reported in Fig. 9.

Both linear and oscillation-based separation strategies were tested employing suitable parameter sets taken from the previous experimental analyses. The laser power was fixed at 6 kW, while a linear scan speed of 80 mm/s was applied. For linear trajectories, the focal position was fixed 10 mm above the surface of the Al-alloy sheet, producing a spot size of 1024 μm . Concerning the oscillation strategy, the beam was focused on the Al-alloy surface to be separated, and circular oscillations with a 1 mm amplitude and a 300 Hz frequency were employed. The tests were conducted by positioning the battery cell and the busbar connector at distances of 10 and 30 mm, given the preliminary nature of this work to provide design guidelines for demanufacturing purposes. In order to verify the resistance to thermal damage of the busbar material, Al with 0.8 mm thickness, Ni-coated steel (Hilumin) with 0.3 mm thickness, and pure Cu with 0.2 mm thickness were tested using both separation strategies. The temperature rise could be measured only for Ni-coated steel and pure Cu, as the thermocouples could not be welded to the Al busbars by capacitor discharge welding due to the low metallurgical compatibility with the thermocouple material. In the linear trajectory experiments, the spot sizes on the busbars were 2032 and 4056 μm at 10 and 30 mm distances, respectively. In the separation experiments with the oscillating beam, the

26 August 2024 08:11:47

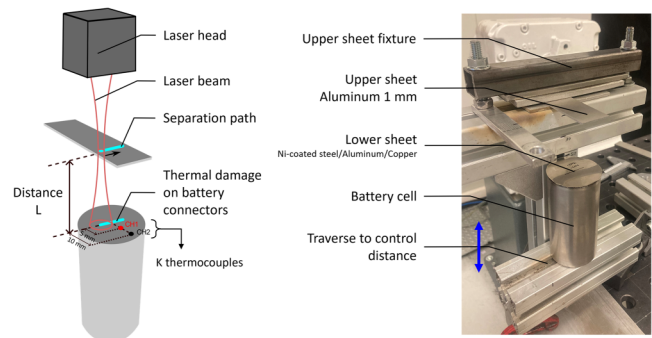


FIG. 9. Schematic description and photograph of the experimental arrangement to measure the temperature rise on the battery cells.

TABLE IV. Fixed and varied parameters used in the separation tests to evaluate the impact on the underlying battery cells.

Fixed parameters	Linear	Oscillation
Power, P (kW)	6	6
Speed, v (mm/s)	80	100
Focal position, Δz (mm)	+10	0
Oscillation amplitude, A (mm)	n/a	1
Oscillation frequency, f (Hz)	n/a	300
Varied parameter	Linear	Oscillation
Distance, L (mm)	10, 30	10, 30

spot sizes on the busbars were 1024 and 3044 μm at 10 and 30 mm distances, respectively. The details of the experimental campaign are summarized in Table IV.

B. Temperature rise on the busbar connections

Figures 10 and 11 show the temperature measurements on Ni-coated steel and pure Cu busbars during the separation process. The results highlight that the separation strategy, the distance from the separation path, and the underlying material have a significant impact on the temperature rise. Overall, higher temperatures are obtained when employing the oscillating separation strategy compared to the linear trajectory, at both 10 and 30 mm distances. In the 10 mm distance configuration, the beam size remains relatively small and the temperature exceeds 800 °C at a 5 mm distance from the path (CH1) on both Ni-coated steel and pure Cu. At the same 10 mm distance, the linear trajectory cuts resulted in temperatures exceeding 400 °C at a 5 mm distance from the path (CH1). At a distance of 30 mm, the linear trajectory increased the temperature levels to approximately 150 °C at a 5 mm distance from the path (CH1) for both materials, while the temperature rose to approximately 300 °C with the oscillating beam. Thermocouples placed at a 10 mm distance from the path (CH2) revealed differences in the heating and cooling behaviors of the two materials. With pure Cu, the temperature rise at a 10 mm distance from the path (CH2) was

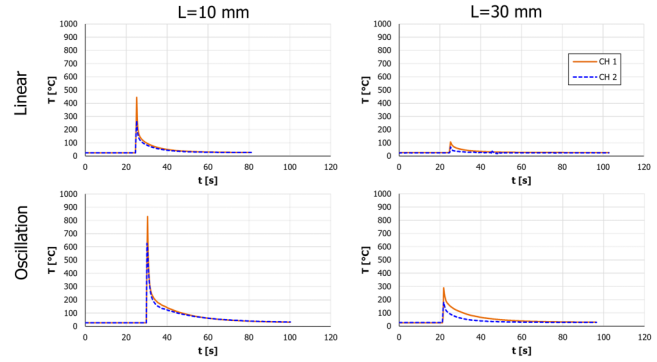


FIG. 11. Temperature rise measured on pure Cu busbars with different cutting strategies and distances measured in two different positions (respectively, channel 1 and channel 2).

more pronounced, highlighting the higher thermal conductivity of the material. The measurements also indicate a faster cooling process with pure Cu with respect to Ni-coated steel.

The temperature measurements indicate a significant temperature increase in the vicinity of the path as shown in Fig. 12, where channel 1 provides higher peak temperatures compared to channel 2. As expected, an increase in the distance between the casing and the underlying busbar (from $L = 10$ mm to $L = 30$ mm) leads to a reduction in the achievable peak temperatures due to the greater defocusing of the process beam. In general, higher peak temperatures are associated with the use of the beam oscillation trajectory while the linear path shows more restricted peak levels. Although such temperatures may generate direct damage to the underlying cell, complete separation of the busbar connector may result in the direct exposure of a cell to the laser beam.

26 August 2024 08:11:47

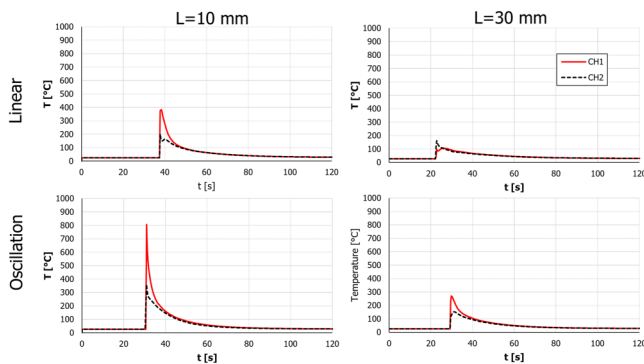


FIG. 10. Temperature rise measured on Ni-coated steel busbars with different cutting strategies and distances measured in two different positions (respectively, channel 1 and channel 2).

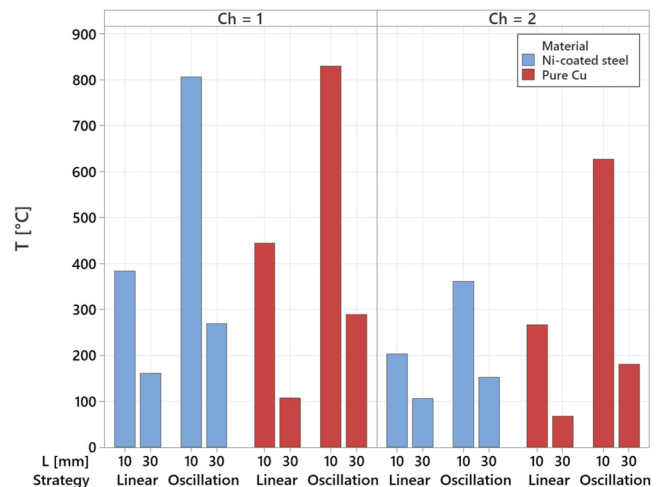


FIG. 12. Peak temperature measured on Ni-coated steel and pure Cu busbars as a function of different distance from the cut surface and different strategies for channel 1 (Ch1) and channel 2 (Ch2).

C. Visual inspection of damage on the busbar connections

The damage status on the tested busbar material as a function of the process parameter is shown in Fig. 13. As seen in Fig. 13(a), all tested conditions resulted in significant damages on the Ni-coated steel busbars. In all cases, partial and full separation occurred, leaving the underlying cell directly exposed to the passing laser beam. The oscillating beam strategy resulted in a larger separation extent compared to the linear trajectory one due to the smaller beam size on the busbar. It should be noted that the maximum temperature values do not fully describe the separation size. Despite having a smaller temperature peak in the oscillation strategy with a 30 mm distance from the busbar, the separation extent is much wider than the linear strategy with a 10 mm distance from the busbar. This implies that a wider beam with oscillating motion can induce a broader damaged region on this material.

Figure 13(b) shows the damage of separation strategies on the pure Cu busbars. It is evident that with a linear trajectory, the damage is limited. High conductivity of the material allows it to dissipate heat without forming an extended melt pool. On the other hand, with the oscillation strategy, the Cu busbars are fully separated at a 10 mm distance. At a higher distance of 30 mm, the beam intensity is reduced, resulting in unstable molten material that is not separated completely. Similar to Ni-coated steel, even with pure Cu, a wider beam at a 30 mm distance can induce a wider damaged region with oscillating motion despite a smaller peak temperature compared to the linear trajectory at 10 mm.

Finally, Fig. 13(c) presents the damage observed on the Al busbars. The images show partial fusion and no effect for the linear trajectory strategy at 10 and 30 mm distances, respectively. Conversely, the oscillation strategy produced complete fusion tracks without separation. While the heat conductivity of Al is higher than that of steel, it is lower than that of Cu. This implies that the separation due to the damage on the busbar depends on the hydrodynamic conditions as well as the thermal conditions during the process.

The damage on the underlying busbar may also be evaluated in terms of the electrical and mechanical properties of the connection. Clearly, in the case of the separation conditions, the busbar connection completely loses its functionality. On the other hand, in the case of partial fusion or no effect observable through optical microscopy, microstructural changes might have occurred in the busbar material. However, a detailed investigation of such aspects goes beyond the scope of the present investigation whose aim was to explore the applicability of a robotic laser welding system for demanufacturing and identifying categorically critical issues. In terms of effects over the underlying battery pack, engineering the laser beam caustic may aid in providing a more defocused beam over the underlying busbar. Moreover, the battery pack design also plays a critical role in determining the amount of damage on the lower sheet. Thus, all of these aspects should be taken into account and investigated further in future works.

V. DISCUSSION

The results demonstrate that both the separation mechanism and damage to the underlying busbars strongly depend on material properties. During laser irradiation, keyhole formation is expected

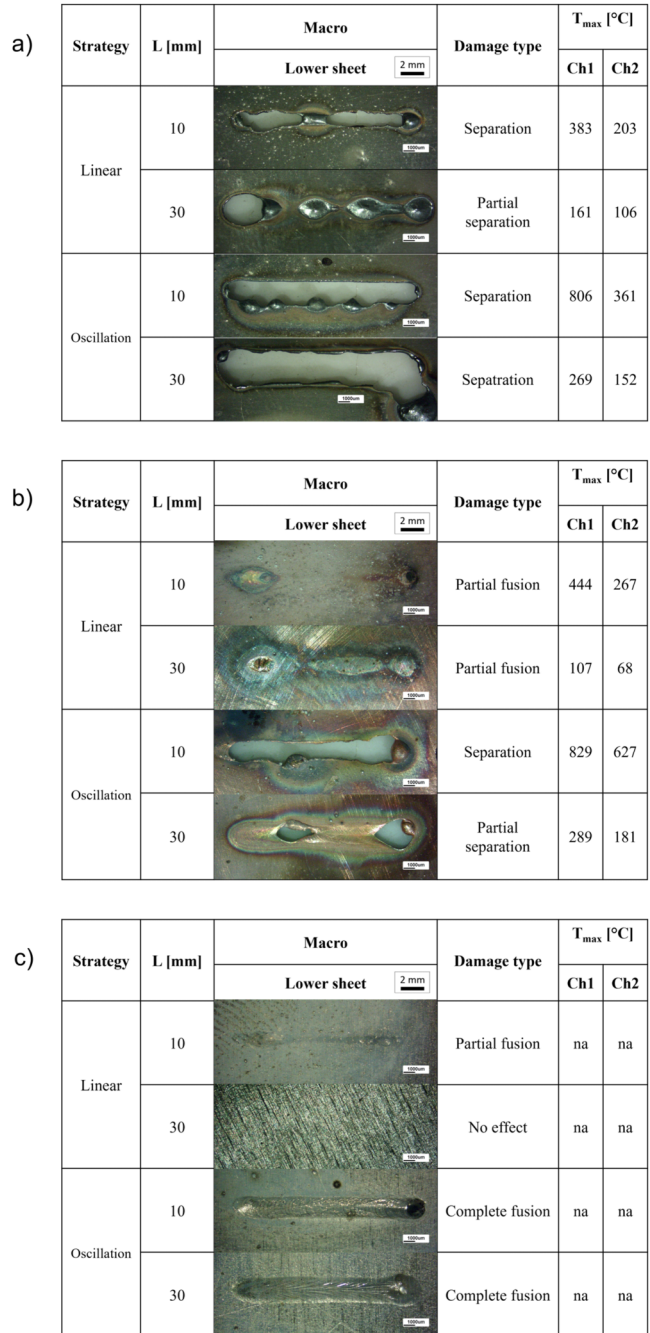


FIG. 13. Optical microscopy images of the underlying busbars showing the different types of damages observed on (a) Ni-coated steel, (b) pure Cu, and (c) Al.

to pierce through the material, while partial vaporization and melting occur laterally to the beam movement. The vaporized material exerts recoil pressure, leading to material splitting and potential expulsion of molten fragments away from the melting

26 August 2024 08:11:47

TABLE V. Main physical properties of the tested metals (Refs. 15 and 42–45).

Parameter	Symbol	Fe	Cu	Al
Density	ρ (kg/m ³)	7870	7190	2700
Heat capacity	c_p (J/kg°C)	460	510	900
Melting temperature	T_m (°C)	1536	1083	660
Boiling temperature	T_b (°C)	2727	2122	2177
Thermal conductivity	k (W/m°C)	50	400	226
Thermal diffusivity	α (m ² /s)	$14 \cdot 10^{-6}$	$109 \cdot 10^{-6}$	$9 \cdot 10^{-6}$
Oxidation enthalpy	ΔH (kJ/mol)	−197	−160	−1675
Viscosity at T_m	η (mPa s)	6.0	4.0	1.3
Surface tension at T_m	γ (N/m)	1.862	1.150	1.050
Optical absorptivity at 1 μm	A	0.35	0.03	0.06
Melting temperature of the oxide	$T_{m,O}$ (°C)	1377 (FeO)	1326 (CuO)	2072 (Al ₂ O ₃)

zone. Material optical absorptivity (A) plays an important role in the power absorbed by the workpiece material. On the other hand, processing in the ambient atmosphere induces oxidation, which may contribute to the process by providing additional energy input. However, successful material expulsion will rely on the pressure field generated as well as material viscosity, surface tension, and kerf opening. Table V collects the physical properties of the materials tested in this study.

Assuming that after the initial keyhole formation the optical absorptivity is increased and comparable, the time required to vaporize the material can be estimated by using a one-dimensional heat propagation model, as expressed by the following equation:

$$t_v = \frac{\pi}{\alpha} \cdot \left(\frac{T_v \cdot k \cdot \pi \cdot d_s^2}{8P} \right)^2, \quad (1)$$

where P is the laser power, d_s is the spot diameter on the material surface, T_v is the vaporization temperature, k is the heat conductivity, and α is the thermal diffusivity.¹⁵ Figure 14 shows the calculated vaporization times as a function of beam size for the tested

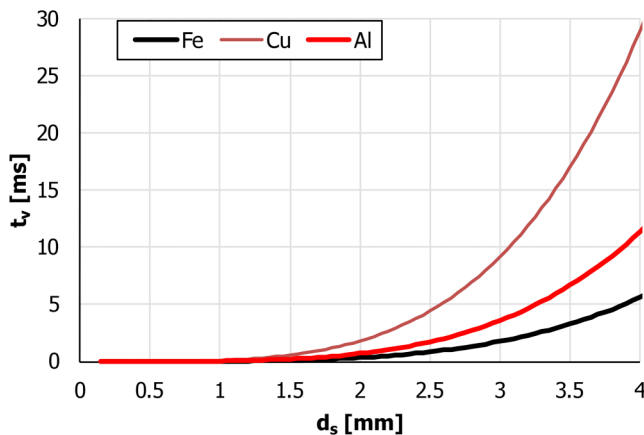


FIG. 14. Calculated vaporization time t_v as a function of laser diameter d_s .

materials. It is evident that for a focused beam with a size of 150 μm , all materials are expected to evaporate instantaneously within ns-range durations. This would correspond to the separated Al alloy with the oscillating beam condition. The vaporization time falls within the microsecond range as the laser beam size increases. That is the case of the linear track cutting strategy on the separated Al alloy that occurs with a 1 mm defocus beam. Regarding the beam reaching the busbars at 10 and 30 mm distances, the beam sizes range between 1 and 3 mm for the oscillating beam and between 2 and 4 mm for the linear track strategy. This leads to vaporization times exceeding 1 ms for the focused beam and reaching several tens of milliseconds for the defocused one.

Due to its lower conductivity compared to Al and Cu, the vaporization of Fe material occurs significantly faster than the other two. This explains how Ni-coated steel is easily damaged in all tested conditions. On the other hand, Al is expected to be easily damaged due to its high oxidation enthalpy and faster vaporization time, although it is lower than Fe but still significantly higher than Cu. However, once aluminum is oxidized and Al₂O₃ is formed, it is expected to act as a heat barrier with low heat conductivity, blocking the kerf extension.

The hydrodynamic conditions may also play a contributing role in the material transport phenomenon. The capillary pressure expressed by the Young–Laplace relationship can be employed for a greater understanding,

$$\Delta p = \frac{\gamma \cos \theta}{w/2}, \quad (2)$$

where γ is the surface tension, θ is the contact angle of the liquid, and w is the kerf width. Assuming a good wetting behavior between the liquid and solid of the same material ($\theta = 0^\circ$), the pressure to expel the melt away from the open kerf can be calculated as seen in Fig. 15. As a preliminary observation, an increase in the kerf size corresponds to a significant drop in the corresponding pressure, leading to an easier separation of the material. While Cu and Al exhibit similarly low levels of capillary pressure, Fe demonstrates a significantly higher one.

Comparing the viscosity of the materials at their respective melting temperatures, it is observed that Fe has the highest value,

26 August 2024 08:11:47

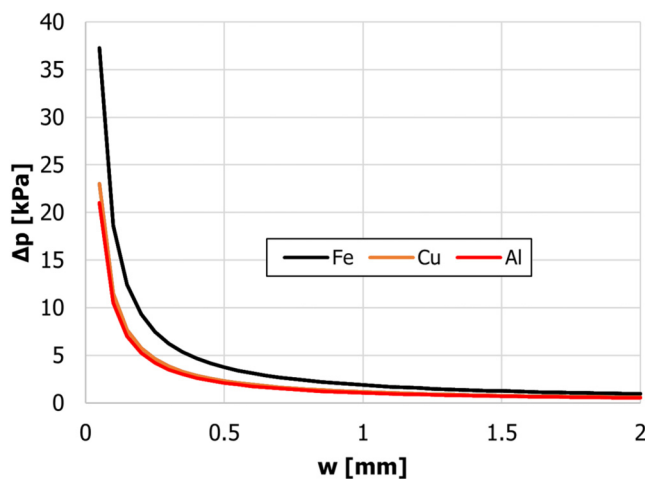


FIG. 15. Calculated capillary pressure Δp as a function of the kerf width w .

followed by Cu, while Al has a much smaller viscosity compared to other materials. Consequently, it can be expected that molten Al will remain fluid, rapidly flowing behind the opened keyhole, and possibly refilling it, while Fe and Cu will possibly not have the same refilling capability. Moreover, Al and its oxide Al_2O_3 exhibit a large gap between their melting temperatures. While the melting temperature of Al is around 660°C , the one of its oxides rises up to 2070°C . Conversely, the melting temperature of FeO is much lower than that of Fe, while Cu and CuO have very close melting temperature values. Hence, it can be assumed that oxide generation should not hinder melt formation for Fe and Cu, while oxide formation for Al is expected to slow down or stop the melting behind the laser-irradiated area. Therefore, it can be hypothesized that the full separation of Fe is the easiest, which has been a cause of damage within this work. Pure Cu resists damage well thanks to its high thermal conductivity. On the other hand, Al and its alloys are expected to be more difficult to separate and damage due to their high melt flowability and high melting temperature of the oxide once it is solidified.

As the separation process was found to potentially cause damage to the underlying material, one strategy is to define the dedicated process trajectories. From this perspective, the use of a robotized system is a fundamental aspect, given the possibility of flexibly reconfiguring the processing conditions while ensuring full accessibility to the workpiece geometry. By avoiding the cells on the separation trajectory or limiting the exposure time, damage can be avoided or confined. Moreover, process reliability and safety as a function of the assembled materials inside the battery pack can be considered. With different battery packs with known materials and architectures, the separation process can be managed by means of the chosen process strategy. Finally, in process monitoring, tools can be integrated to sense the change of the process material and regulate the parameters accordingly. The sensors integrated for the welding process such as inline photodiodes^{46,47} and optical coherence tomography^{48,49} can be readily used. External sensors such as thermal cameras can also be a complementary solution to verify the thermal overload on the battery pack.⁵⁰

IV. CONCLUSIONS

In this work, the use of a remote laser separation process was studied to assess its suitability for recycling battery packs. The work proposed linear and oscillation trajectories to separate thin sheets of Al alloys, representative of the battery pack container, in the absence of a process assistant gas. A laser system designed for welding applications was employed. The work showed that kerf widening is required to achieve complete separation on the Al alloy for which a highly defocused beam or widely oscillated focused beam is required. In the full separation conditions, the laser light passes through the open kerf, hitting the underlying materials that can be the busbar or the cell itself. An experimental setup was designed and implemented to study the possible effects of the excess laser beam on the busbars and, possibly, on the cells to be recovered. The measurements provide temperature data as well as damage types. The overall results show that the approach is feasible, while a careful process trajectory planning should be considered, which can be assisted by means of inline process monitoring tools.

ACKNOWLEDGMENTS

The authors are thankful to the BLM Group for the longstanding collaboration. The Italian Ministry of Education, University and Research (MIUR) is acknowledged for the support provided through the National Plan of Recovery and Resilience (PNRR).

AUTHOR DECLARATIONS

Conflict of Interest

The authors have no conflicts to disclose.

Author Contributions

Simone D'Arcangelo: Conceptualization (equal); Data curation (equal); Formal analysis (equal); Investigation (equal); Methodology (equal); Writing – original draft (equal); Writing – review & editing (equal). **Matteo Busatto:** Conceptualization (equal); Methodology (equal); Writing – review & editing (equal). **Leonardo Caprio:** Conceptualization (equal); Methodology (equal); Writing – original draft (equal); Writing – review & editing (equal). **Barbara Previtali:** Conceptualization (equal); Methodology (equal); Resources (equal); Writing – original draft (equal); Writing – review & editing (equal). **Ali Gökhan Demir:** Conceptualization (equal); Formal analysis (equal); Investigation (equal); Methodology (equal); Supervision (equal); Writing – original draft (equal); Writing – review & editing (equal).

REFERENCES

- ¹A. G. Demir, J. Kriegler, A. Fortunato, L. Caprio, C. Geiger, L. Hille, *et al.*, “Challenges and opportunities for laser applications in electric vehicle manufacturing,” in *Selected Topics in Manufacturing: Emerging Trends from the Perspective of AITeM's Young Researchers*, edited by L. Carrino, L. M. Galantucci, and L. Settineri (Springer, Cham, Switzerland, 2023), pp. 219–253.
- ²M. Rettenmeier, M. Möller, O. Bocksrocker, V. Salvarrajan, and C. Neugebauer, “Battery recycling—Exploitation of laser technologies for dismantling and recycling processes,” in *Lasers in Manufacturing Conference*, 2023.
- ³W. Pfleging, “A review of laser electrode processing for development and manufacturing of lithium-ion batteries,” *Nanophotonics* 7, 549–573 (2018).

- ⁴Y. Zhang, J. Li, R. Yang, T. Liu, and Y. Yan, "Analysis of kerf quality on ultrafast laser cutting of anode material for lithium-ion battery," *Opt. Lasers Eng.* **118**, 14–21 (2019).
- ⁵A. H. A. Lutey, A. Fortunato, S. Carmignato, A. Ascari, E. Liverani, and G. Guerrini, "Quality and productivity considerations for laser cutting of LiFePO₄ and LiNiMnCoO₂ battery electrodes," *Proc. CIRP* **42**, 433–438 (2016).
- ⁶A. H. A. Lutey, A. Fortunato, S. Carmignato, and M. Fiorini, "High speed pulsed laser cutting of Li-ion battery electrodes," *Opt. Laser Technol.* **94**, 90–96 (2017).
- ⁷A. G. Demir and B. Previtali, "Remote cutting of Li-ion battery electrodes with infrared and green ns-pulsed fibre lasers," *Int. J. Adv. Manuf. Technol.* **75**, 1557–1568 (2014).
- ⁸J. Krieglger, M. Binzer, and M. F. Zaeh, "Process strategies for laser cutting of electrodes in lithium-ion battery production," *J. Laser Appl.* **33**, 012006 (2021).
- ⁹R. Patwa, H. Herfurth, S. Heinemann, J. Mazumder, and D. Lee, "Investigation of different laser cutting strategies for sizing of Li-ion battery electrodes," in *International Congress on Applications of Lasers and Electro-Optics* (Laser Institute of America, Orlando, FL, 2012), pp. 908–914.
- ¹⁰D. Lee, R. Patwa, H. Herfurth, and J. Mazumder, "Parameter optimization for high speed remote laser cutting of electrodes for lithium-ion batteries," *J. Laser Appl.* **28**, 022006 (2016).
- ¹¹D. Lee, R. Patwa, H. Herfurth, and J. Mazumder, "High speed remote laser cutting of electrodes for lithium-ion batteries: Anode," *J. Power Sources* **240**, 368–380 (2013).
- ¹²D. Lee and J. Suk, "Laser cutting characteristics on uncompressed anode for lithium-ion batteries," *Energies (Basel)* **13**, 2630 (2020).
- ¹³J. Huang, W. Shi, J. Huang, Y. Xie, Y. Ba, and K. He, "High speed pulsed laser cutting of anode material for a Li-ion battery in burst mode," *Opt. Mater. Express* **11**, 2300 (2021).
- ¹⁴M. Lütke, F. Bartels, J. Hauptmann, A. Wetzig, and E. Beyer, "The energetic efficiency of remote cutting in comparison to conventional fusion cutting," in *30th International Congress on Applications of Lasers and Electro-Optics, ICALEO 2011* (Laser Institute of America, Orlando, FL, 2011), pp. 16–24.
- ¹⁵W. M. Steen and J. Mazumder, *Laser Material Processing* (Springer London, London, 2010).
- ¹⁶M. Naeem and S. Lewis, "Micro joining and cutting with a single mode fiber laser," in *Proceedings of the 2nd Pacific International Conference on Application of Lasers and Optics* (Laser Institute of America, Orlando, FL, 2006).
- ¹⁷A. Wetzig, P. Herwig, J. Hauptmann, R. Baumann, P. Rauscher, M. Schlosser, T. Pinder, and C. Leyens, "Fast laser cutting of thin metal," *Proc. Manuf.* **29**, 369–374 (2019).
- ¹⁸A. Pihlava, T. Purtonen, A. Salminen, V. Kujanpää, and T. Savinainen, "Quality aspects in remote laser cutting," *Weld. World* **57**, 179–187 (2013).
- ¹⁹R. Baumann, A. F. Lasagni, P. Herwig, A. Wetzig, C. Leyens, and E. Beyer, "Efficient separation of battery materials using remote laser cutting—high output performance, contour flexibility, and cutting edge quality," *J. Laser Appl.* **31**, 022210 (2019).
- ²⁰M. Lütke, A. Mahrle, T. Himmer, L. Morgenthal, and E. Beyer, "Remote-cutting—A smart solution using the advantages of high brightness lasers," in *International Congress on Applications of Lasers & Electro-Optics* (Laser Institute of America, Orlando, FL, 2008).
- ²¹G. F. Antonova, G. G. Gladush, A. G. Krasnyukov, F. K. Kosyrev, and N. B. Rodionov, "The mechanism of remote cutting of metals by CO₂-laser radiation," *High Temp.* **38**, 477–482 (2000).
- ²²V. G. Vostrikov, V. D. Gavriluk, A. G. Krasnyukov *et al.*, "Mobile laser technological complex MLTK-50 for remote cutting of metal structures," *Chem. Pet. Eng.* **37**, 308–311 (2001).
- ²³G. G. Gladush and I. Smurov, *Physics of Laser Materials Processing: Theory and Experiment* (Springer Science & Business Media, Berlin, 2011), Vol. 146.
- ²⁴A. Brodessa, C. Hennigs, A. Pfaff, R. Graf, M. Hustedt, and S. Kaierle, "Demonstration of a mobile laser cutting system for complex rescue operations," *J. Laser Appl.* **31**, 022209 (2019).
- ²⁵A. Choubey, R. K. Jain, S. Ali *et al.*, "Studies on pulsed Nd:YAG laser cutting of thick stainless steel in dry air and underwater environment for dismantling applications," *Opt. Laser Technol.* **71**, 6–15 (2015).
- ²⁶S. L. Villumsen, M. Kristiansen, and F. O. Olsen, "On the stability and performance of remote DOE laser cutting," *Phys. Proc.* **83**, 1206–1216 (2016).
- ²⁷S. L. Villumsen and M. Kristiansen, "Investigation of cutting quality of remote DOE laser cutting in 0.5 mm stainless steel," *Phys. Proc.* **89**, 164–171 (2017).
- ²⁸S. Villumsen and M. Kristiansen, "Angular stability margins for the remote fusion cutting process," *Phys. Proc.* **78**, 89–98 (2015).
- ²⁹S. Villumsen, S. N. Joergensen, and M. Kristiansen, "Flexible laser metal cutting: An introduction to the ROBOCUT laser cutting technique," in *Proceedings of the 7th World Conference on Mass Customization, Personalization, and Co-Creation (MCPC 2014), Aalborg, Denmark, 4–7 February 2014*, Twenty Years of Mass Customization—Towards New Frontiers (Springer, Cham, Switzerland, 2014), pp. 217–228.
- ³⁰A. Wagner, M. Lütke, A. Wetzig, and L. M. Eng, "Laser remote-fusion cutting with solid-state lasers," *J. Laser Appl.* **25**, 052004 (2013).
- ³¹M. Lütke, A. Wagner, A. Wetzig, and E. Beyer, "Identification and characterization of analogies of remote fusion cutting processes using different beam sources," in *International Congress on Applications of Lasers & Electro-Optics* (Laser Institute of America, Orlando, FL, 2012), pp. 292–301.
- ³²M. F. Zaeh, J. Moesl, J. Musiol, and F. Oefele, "Material processing with remote technology—Revolution or evolution?," *Phys. Proc.* **5**, 19–33 (2010).
- ³³J. Hatwig, P. Minnerup, M. F. Zaeh, and G. Reinhart, "Automated task planning for industrial robots and laser scanners for remote laser beam welding and cutting," in *2012 IEEE International Conference on Mechatronics and Automation* (IEEE, New York, 2012).
- ³⁴A. Schober, J. Musiol, R. Daub, J. Feil, and M. F. Zaeh, "Experimental investigation of the cutting front angle during remote fusion cutting," *Phys. Proc.* **39**, 204–212 (2012).
- ³⁵M. Kardan, N. Levichev, and J. R. Dufloy, "Experimental and numerical investigation of thick plate laser cutting using dynamic beam shaping," *Proc. CIRP* **111**, 740–745 (2022).
- ³⁶M. Kardan, N. Levichev, S. Castagne, and J. R. Dufloy, "Cutting thick aluminum plates using laser fusion cutting enhanced by dynamic beam shaping," *J. Laser Appl.* **35**, 042074 (2023).
- ³⁷M. Kardan, N. Levichev, S. Castagne, and J. R. Dufloy, "Dynamic beam shaping requirements for fiber laser cutting of thick plates," *J. Manuf. Process.* **103**, 287–297 (2023).
- ³⁸N. Levichev, M. R. Vetrano, and J. R. Dufloy, "Melt flow and cutting front evolution during laser cutting with dynamic beam shaping," *Opt. Lasers Eng.* **161**, 107333 (2023).
- ³⁹M. Sawannia, M. Borkmann, P. Herwig, A. Wetzig, C. Hagenlocher, and T. Graf, "Influence of beam oscillation on the melt flow during laser beam fusion cutting and the resulting cut quality," in *Lasers in Manufacturing Conference*, 2032, pp. 26–29.
- ⁴⁰N. Levichev, P. Herwig, A. Wetzig, and J. R. Dufloy, "Towards robust dynamic beam shaping for laser cutting applications," *Proc. CIRP* **111**, 746–749 (2022).
- ⁴¹A. Kampker, S. Wessel, F. Fiedler, and F. Maltoni, "Battery pack remanufacturing process up to cell level with sorting and repurposing of battery cells," *J. Remanuf.* **11**, 1–23 (2021).
- ⁴²E. Yousefi, Y. Sun, A. Kunwar, M. Guo, N. Moelans, and D. Seveno, "Surface tension of aluminum-oxygen system: A molecular dynamics study," *Acta Mater.* **221**, 117430 (2021).
- ⁴³M. Wu, A. H. Caldwell, and A. Allamore, "Surface tension of high temperature liquids evaluation with a thermal imaging furnace," in *Minerals, Metals and Materials Series* (Springer International, Cham, Switzerland, 2019), pp. 33–41.
- ⁴⁴A. T. Dinsdale and P. N. Queded, "The viscosity of aluminum and its alloys—A review of data and models," *J. Mater. Sci.* **39**, 7221–7228 (2004).

- ⁴⁵V. Klapczynski, D. Le Maux, M. Courtois, E. Bertrand, and P. Paillard, "Surface tension measurements of liquid pure iron and 304L stainless steel under different gas mixtures," *J. Mol. Liq.* **350**, 118558 (2022).
- ⁴⁶M. Garavaglia, A. G. Demir, S. Zarini, B. M. Victor, and B. Previtali, "Fiber laser welding of AA 5754 in the double lap-joint configuration: Process development, mechanical characterization, and monitoring," *Int. J. Adv. Manuf. Technol.* **111**, 1643–1657 (2020).
- ⁴⁷L. Caprio, B. Previtali, and A. G. Demir, "Sensor selection and defect classification via machine learning during the laser welding of busbar connections for high-performance battery pack production," *Lasers Manuf. Mater. Process.* **11**(2), 329–352 (2024).
- ⁴⁸C. Stadter, M. Schmoeller, L. von Rhein, and M. F. Zaeh, "Real-time prediction of quality characteristics in laser beam welding using optical coherence tomography and machine learning," *J. Laser Appl.* **32**, 022046 (2020).
- ⁴⁹C. Mittelstädt, T. Mattulat, T. Seefeld, and M. Kogel-Hollacher, "Novel approach for weld depth determination using optical coherence tomography measurement in laser deep penetration welding of aluminum and steel," *J. Laser Appl.* **31**, 022007 (2019).
- ⁵⁰M. Grasso, A. G. Demir, B. Previtali, and B. M. Colosimo, "In situ monitoring of selective laser melting of zinc powder via infrared imaging of the process plume," *Robot. Comput. Integr. Manuf.* **49**, 229–239 (2018).